Original Article

Phase formation prediction of high-entropy alloys: a deep learning study

Check for updates

Wenhan Zhu [a,b], **Wenyi Huo** [a,*], **Shiqi Wang** [c], **Xu Wang** [a], **Kai Ren** [a], **Shuyong Tan** [d], **Feng Fang** [c], **Zonghan Xie** [e], **Jianqing Jiang** [a,c]

[a] School of Mechanical and Electrical Engineering, Nanjing Forestry University, Nanjing 210037, China
[b] Changzhou Leiding Intelligent Technology Co., Ltd., Changzhou 213017, China
[c] Jiangsu Key Laboratory of Advanced Metallic Materials, Southeast University, Nanjing 211189, China
[d] School of Materials Science and Engineering, Nanjing Institute of Technology, Nanjing 211167, China
[e] School of Mechanical Engineering, University of Adelaide, SA 5005, Australia

ARTICLE INFO

ABSTRACT

High-entropy alloys (HEAs) represent prospective applications considering their outstanding mechanical properties. The properties in HEAs can be affected by the phase structure. Artificial neural network (ANN) is a promising machine learning approach for predicting the phases of HEAs. In this work, a deep neural network (DNN) structure using a residual network (RESNET) is proposed for the phase formation prediction of HEAs. It shows a high overall accuracy of 81.9%. Compared it with machine learning models, e.g., ANN and conventional DNN, its Micro-F1 score highlights the advantages of phase prediction of HEAs. It can remarkably prevent network degradation and improve the algorithm accuracy. It delivers a new path to develop the phase formation prediction model using deep learning, which can be of universal relevance in assisting the design of the HEAs with novel chemical compositions.

1. Introduction

High-entropy alloys (HEAs) are a newly promising kind of material with outstanding properties [1–3]. It typically shows complex chemical composition with multiple components [4]. Phase engineering is proposed to obtain excellent performance combinations via different phase structures in HEAs [5]. Via phase engineering, HEAs can exhibit high hardness [6], high strength [7], high ductility [8], strong wear resistance [9], strong corrosion resistance [10], and superior catalytic properties [11]. These three phases, solid solution (SS), amorphous (AM), and intermetallic (IM), are found and indexed in HEAs. The phase structure remarkably affects the properties of HEAs. Despite the advances that have been made in the field of high-entropy alloy phase formation, it still exhibits a complex and time-consuming design process. Notably, machine learning has been recognized as a useful method to aid material design [12].
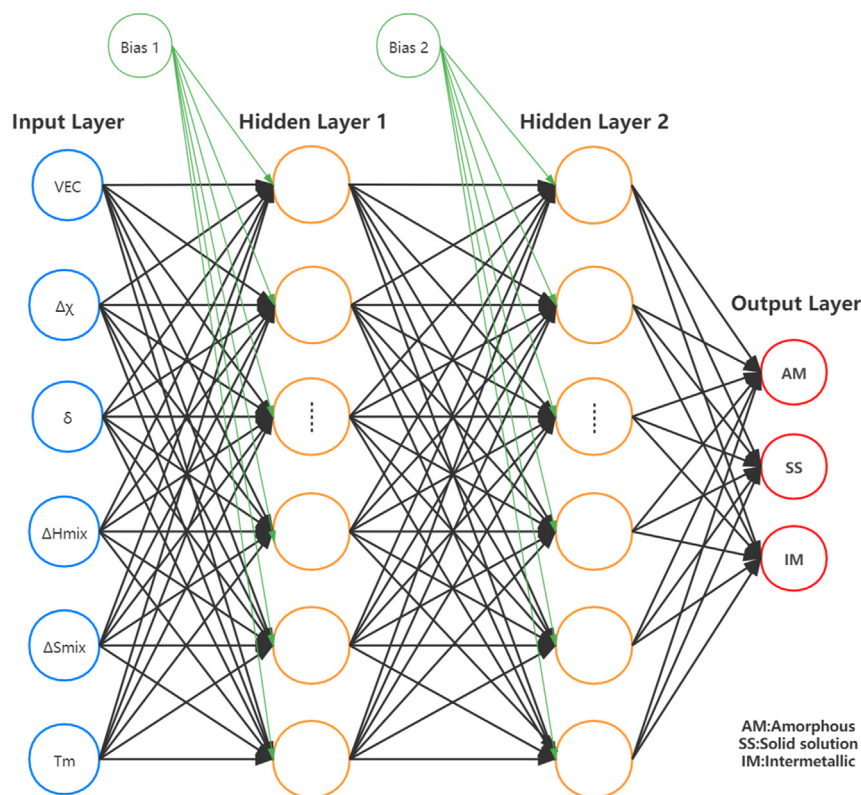
Fig. 1 − Schematic diagram of the ANN model for phase formation prediction of HEAs.

Machine learning, e.g., deep learning, is a type of artificial intelligence. It extracts features from a large number of datasets, and summarizes the relationships among them. The available data in the existing works about HEAs provides opportunities to use different deep learning algorithms for the phase formation prediction of HEAs. With both the data accumulation of HEAs and the development of deep learning algorithms, several works show interesting results for the phase formation prediction of HEAs. This shows that it is a promising method for the prediction of HEAs [13−15]. It shows a deep learning method to predict the hardness of refractory HEAs with excellent accuracy for the first time in Uttam et al.'s work [16]. The algorithms include support vector machine (SVM) classifier, logistic regression, gradient boosting classifier, decision trees, artificial neural network (ANN), and random forest to predict the phases of HEAs in Yegi et al.'s work [17]. It shows the methods containing K-nearest neighbors (KNN), SVM, and ANN to forecast the phases in Huang et al.'s work [18]. It shows that the method of ANN is more precise than the others. Therefore, there is the promising future for using neural networks to forecast phases in HEAs. Islam et al.'s work [19] shows an ANN method to predict phases and it shows that the training set accuracy might be as high as 99% while the actual prediction accuracy was less than 80%. Notably, it is important for the HEA design to enhance the predictive performance. Although there are many results in this rapidly growing field, there are still some challenges in the phase prediction of HEAs, e.g., the optimization of deep learning algorithms and the limited amount of experimental data. There will be a large number of unstudied HEA compositions for a long time, since the compositional design space for HEAs is enormous. It is crucial to propose high-performance deep learning algorithms based on existing available data for the phase prediction of HEAs.

Herein, it shows a mixed deep neural network (DNN) and residual network (RESNET) architecture to train the best suitable model for the current dataset by constantly optimizing the hyperparameters, e.g., the minibatch size, learning rate, learning rate decay, dropout rate, for phase formation prediction of HEAs. The significance of the feature parameters is evaluated on the phase prediction outcomes. The Micro-F1 score is applied to compare the results to those of the ANN and DNN on the final test set.

2. Methods

2.1. Data collection

The HEA data of are preprocessed using a traditional data science method before training the architecture. Five separate datasets from many prior studies [20−24] are selected and used for the establishment of the deep-learning-based phase prediction model. After eliminating redundant samples and portions with missing data, it offered a dataset of 529 HEAs containing 131 AM, 196 SS, and 202 IM phases.
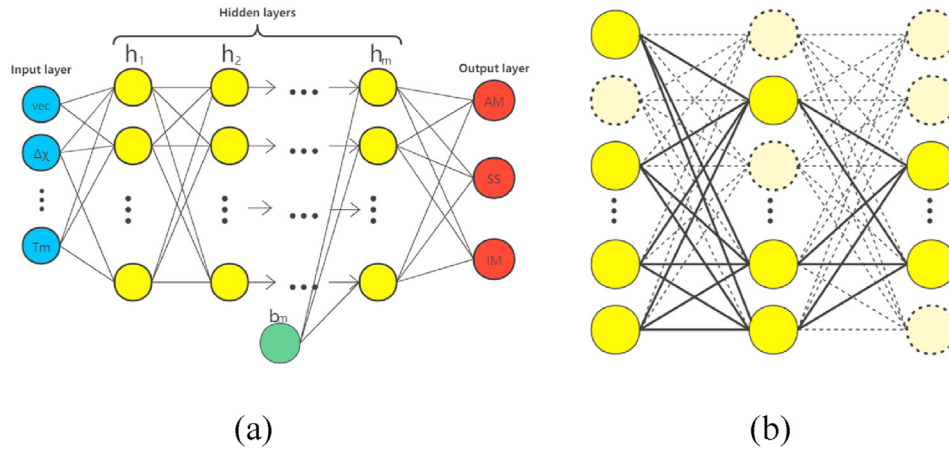
Fig. 2 − Schematic diagram of the DNN model for the phase formation prediction of HEAs. (a) A deep neural network is made up of an input layer, multiple hidden layers, and one output layer. (b) Random interconnections of neurons in the hidden layers are regulated by the dropout technique.

After the labels for phases are verified, the NN model is extracted, and the features are evaluated. Six relevant features, including valence electron concentration (VEC), electronegativity difference ($\Delta\chi$), atomic size difference (δ), mixing enthalpy (ΔH_{mix}), mixing entropy (ΔS_{mix}), and melting temperature (T_m), are selected based on domain knowledge of which features could be useful in phase prediction. The input numerical values for the six features are derived from the formulae below [25−28],

$$VEC = \sum_{i=1}^{n} c_i VEC_i \tag{1}$$

$$\Delta\chi = \sqrt{\sum_{i=1}^{n} c_i (\chi_i - \overline{\chi})^2} \tag{2}$$

$$\delta = 100 \times \sqrt{\sum_{i=1}^{n} c_i (1 - r_i/\overline{r})^2} \tag{3}$$

$$\Delta H_{mix} = \sum_{i=1,i<j}^{n} 4 H_{ij} c_i c_j \tag{4}$$

$$\Delta S_{mix} = -R \sum_{i=1}^{n} c_i \ln c_i \tag{5}$$

$$T_m = \sum_{i=1}^{n} c_i T_{mi} \tag{6}$$

where c_i ($0 < c_i < 1$) denotes the atomic concentrations for the i th element. n represents the total number of components in an HEA. VEC_i stands for the valence electron concentration of the i th element. H_{ij} is the enthalpy of atomic pairs computed by Miedema's model [29]. T_{mi}, χ_i and r_i are the melting point, Pauling electronegativity and atomic radius of the i th element, respectively. The averaged Pauling electronegativity is $\overline{\chi}$, and the averaged atomic radius is $\overline{r}$. The averaged Pauling electronegativity $\overline{\chi}$ is computed as $\overline{\chi} = \sum_{i=1}^{n} c_i \chi_i$, and the

averaged atomic radius $\overline{r}$ is calculated as $\overline{r} = \sum_{i=1}^{n} c_i r_i$. R refers to the gas constant.

2.2. ANN and DNN

In the ANN, the neurons that perform computational functions collectively constitute a layer. It describes the a_j that means the output of every neuron in the hidden layer as follows,

$$a_j = \sum_{i=1}^{n} x_i W_{ij} + b_j \tag{7}$$

where W_{ij} denotes the weights assigned to every of the input parameters x_i and b_j refers to the bias coefficients. The ANN model with backpropagation functions depicted in Fig. 1 consists of two hidden layers, each of which contains 20 neurons. The value of a_j is obtained via Eq. (7) from each neuron linked with connection-specific weights. It feed the value into the activation function. The input layer contains six parameters for features, and the output layer consists of 3 neurons that signify the phases.

A DNN is an architecture that enhances the number of neurons and hidden layers as shown in Fig. 2a, which is based on an ANN. The dropout strategy is used to eliminate overfitting, as shown in Fig. 2b. It updates the weights of the neural network utilizing Eq. (7) while keeping the input and output layers unaltered. After expanding from the ANN, there are 6 hidden layers, and each layer holds 20 neurons.

2.3. RESNET

In Fig. 3, the RESNET model shows the architecture with skip connections. As the scale of the layers in the training network is enhanced, the degradation of the network and a decrease in accuracy inevitably occur. The residual units resolve the degradation and gradient troubles. It adds the values of the upper layer to the current layer and transmits it as the input for the next layer or the far layer as follows,
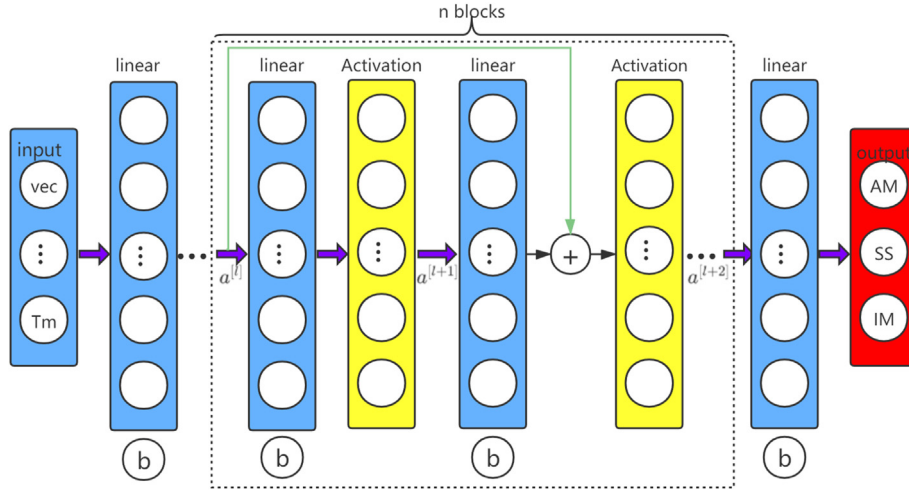
Fig. 3 – Schematic diagram of the RESNET model for the phase formation prediction of HEAs.

$$a^{[l+2]} = g\left(wa^{[l+1]} + b + a^{[l]}\right) \tag{8}$$

where $g(\cdot)$ is the activation function, and $a^{[l]} \to a^{[l+2]}$ are the hidden layers. The residual blocks that feed the parameter of some layer into the later hidden layer can aid in resolving network degradation.

2.4. Deep learning

Before training the architecture, the data are processed for the feature values. The feature values are normalized, and the values are varied between 0 and 1 with the Pandas library, as below,

$$X_{\text{new}} = \frac{X_i - X_{\text{min},i}}{X_{\text{max},i} - X_{\text{min},i}} \tag{9}$$

where X_i denotes the original information about the features, $X_{\text{min},i}$ and $X_{\text{max},i}$ signify the minimum and maximum values, respectively. X_{new} refers the normalized feature. The purpose of normalization is to provide a dimensionless numerical representation. The procedure guarantees features with the same numeric weight. Among the features, they are evaluated equally.

There are three neurons that represent the AM, SS and IM in the output layer and the SoftMax activation function is commonly employed in the task of classification. The function for the type of multiple classification is considered as the final activation function since there are three final classification results. In contrast to the target labels and the actual output value, the error of the network is calculated via the cross-entropy loss function. The gradient descent technique with learning rate is used to transmit the mistake back to the architecture. At the initial stage of the training procedure, the weights and bias are initialized with seeds and updated. The SoftMax [30] function and cross-entropy [31] loss function are as follows:

$$\sigma(y_i') = \frac{e^{y_i'}}{\sum\limits_{i=1}^{n} e^{y_i'}} \tag{10}$$

$$H_y(y') = -\sum_{i=1}^{n} y \log(\sigma(y_i')) \tag{11}$$

where y refers to one of the One-Hot encoders, y' signifies the prediction, and $\sigma(y_i')$ is the probability. The neural network's final output is translated into probability and used to calculate loss via cross-entropy.

The model is trained with the training set, and assessed with the validation set. Its parameters are modified by delivering feedback based on the results of the validation set. The preferred model with the best results on the validation set is obtained. The model is checked using the test set. Finally, the hyperparameters are shown in Table 1.

3. Results and discussions

3.1. Data analysis

Fig. 4 shows the 6×6 scatter matrix plot showing the dataset. The subgraphs on the diagonal show the histograms of the phase distribution with only one feature from the six features. It shows that, no individual feature can be adopted to properly identify the alloy phases, since all of the histograms in each subgraph cannot be isolated from one another. The subgraphs that are drawn on the off-diagonal mean that the phase selection depends on the correlations among the six features. This indicates that a single feature cannot be used to distinguish these phases.

To describe the correlation between the values of six features, the Pearson correlation coefficients are derived from the formula below [32],

$$r_{xy} = \frac{1}{n-1} \frac{\sum\limits_{i=1}^{n}(x_i - \bar{x}) - (y_i - \bar{y})}{\sigma_x \sigma_y} \tag{12}$$

where n represents the total number, $\bar{x}$ and $\bar{y}$ are the mean values of two input features, and σ_x or σ_y, are the standard

Table 1 – Hyperparameters of ANN, DNN, and DNN with RESNET.

Model	ANN	DNN	DNN + RESNET
Number of hidden layers	2	10	DNN(6)+ RESNET (2)
Number of hidden neurons	20	20	20
Minibatch size	8, 16, 32, 64	8, 16, 32, 64	8, 16, 32, 64
Learning rate decay coefficient	0.1, 0.5	0.1, 0.5	0.1, 0.5
Learning rate	0.1, 0.01, 0.001	0.1, 0.01, 0.001	0.1, 0.01, 0.001
Dropout rate	0.3, 0.5, 0.7	0.3, 0.5, 0.7	0.3, 0.5, 0.7
Activation	Relu, Leaky Relu	Relu, Leaky Relu	Relu, Leaky Relu
Epoch	100–200	100–200	100–200
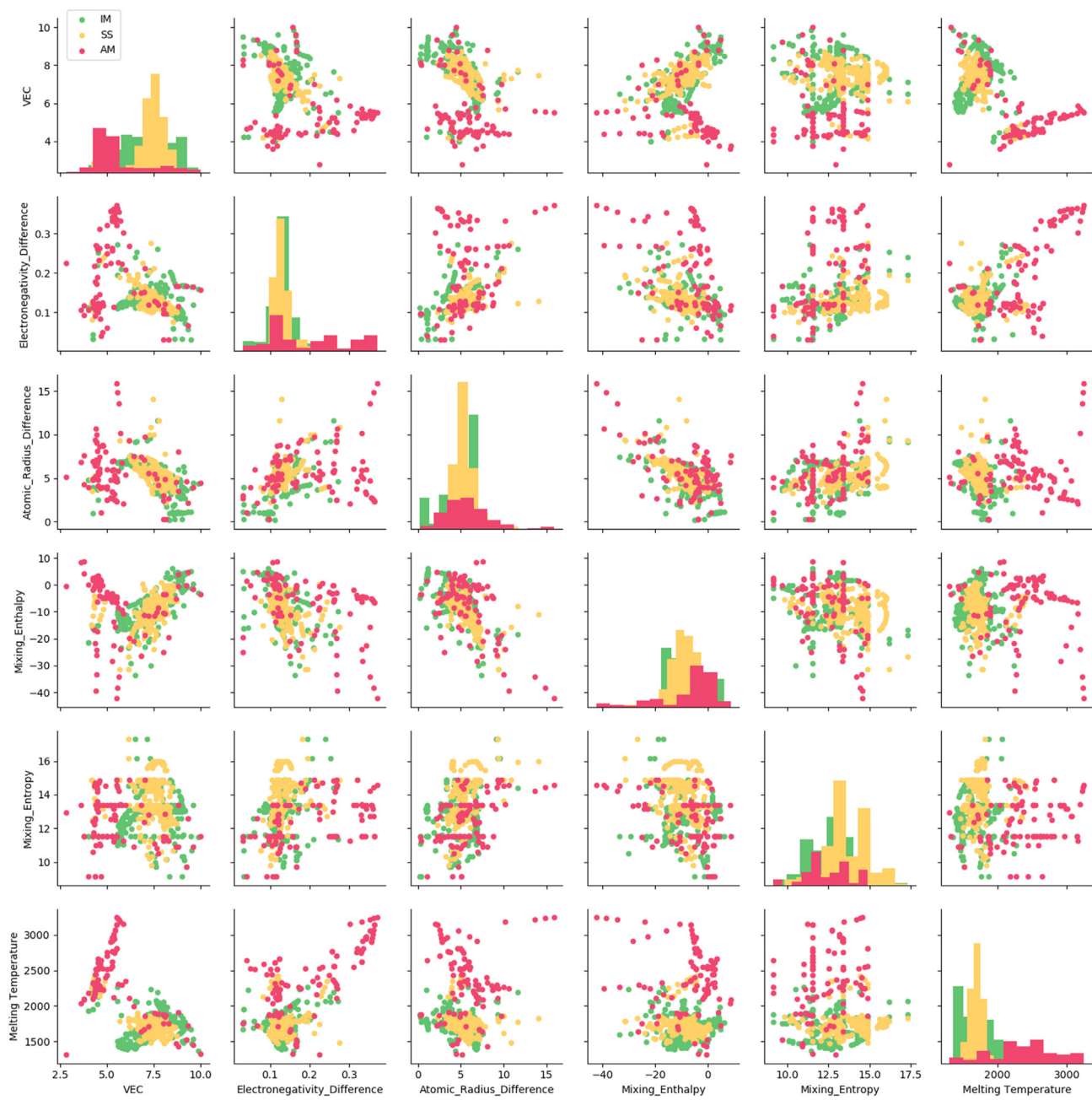
Fig. 4 – Green stands for IM, yellow refers to SS, and red is AM. The diagonal histogram in the diagonal panels depicts distributions of the three phases with the different six features. The scatter plots in the off-diagonal panels show the correlation of the values for the different six features.
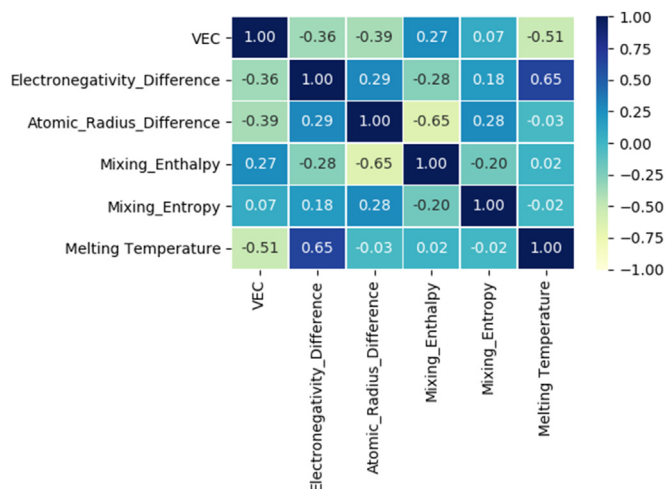
Fig. 5 − Heatmap of the correlation matrix between the six features.

deviations of the two features. The values that are used to describe the correlations quantitatively vary from 1 to −1, indicating a highly positive or negative relationship. The feature correlations calculated by Eq. (12) are shown in Fig. 5.

As shown in Fig. 5, the matrix elements range from −0.65 to 0.65 when paying attention to the correlation between two separate features. We can understand from the fifty independent correlation matrix members that seven of them are positive, and the others are negative. In accordance with Fig. 5, the atomic size difference and mixing enthalpy show a negative correlation, which it means that the atomic size difference appears larger as the mixing enthalpy decreases. The electronegativity difference and melting temperature correlate positively. Overall, no strong positive or negative correlation matrix exists between any two features, implying that the six features should be taken into account in the deep learning model.

The dataset is generally divided into a training set and a test set throughout the machine learning modeling process.

The test set unrelated to the training is not used in any manner during the training and is used to evaluate the final model. In this work, 4-fold cross-validation is used, as shown in Fig. 6.

3.2. Deep learning results

All Python network models are built in the Keras (TensorFlow backend) deep learning framework. The dataset is split into subsets. The subsets of ANN and DNN are trained using gradient descent. The values of the hyperparameters are then updated. The optimum model and hyperparameter values for the ANN and DNN are obtained by 4-fold cross-validation, as shown in Table 2.

In Fig. 7, it shows the results of ANN and DNN. Overall accuracy improves as training times rise. This shows that the accuracy of the ANN oscillates more, which is caused by the small minibatch size. With the decline in the learning rate,
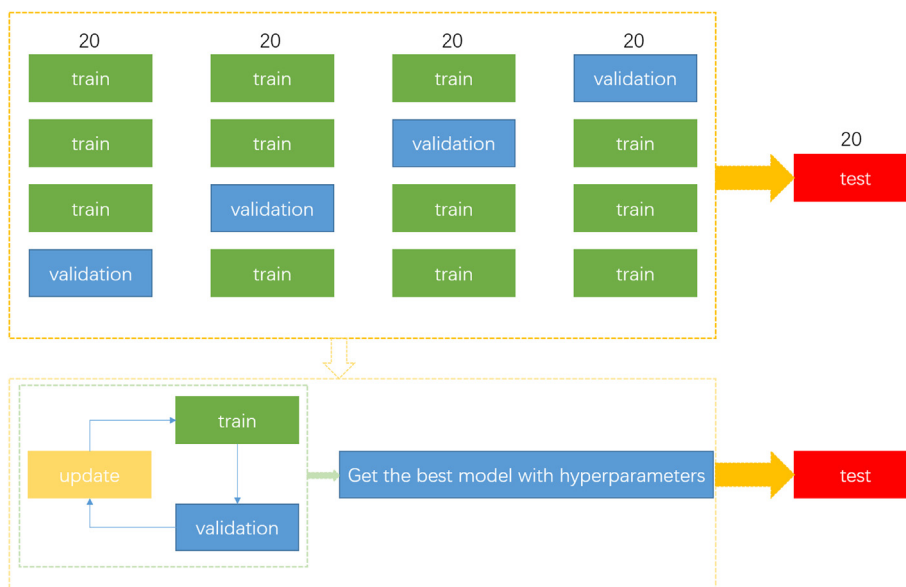

Fig. 6 − Processing of training and testing the neural network.

Table 2 – Appropriate parameters of ANN, DNN.

Model	ANN	DNN
Number of hidden layers	2	10
Number of hidden neurons	20	20
Minibatch size	8	64
Learning rate decay coefficient	0.5	0.3
Learning rate	0.01	0.001
Dropout rate	0.5	0.3
Activation	Relu	Relu
Epoch	100	100

the oscillation decreases gradually. Islam et al. [19] proposed that a neural network with two hidden layers leads to overfitting due to the limited number of neurons in the hidden layers. The accuracy of the validation set is not substantially improved despite increasing the number of neurons and introducing dropout. This suggests that the neural network limits the number of layers, which causes the features to be learned in each layer to be complicated. If there are multiple layers, the feature information and classification information can be retrieved hierarchically. As seen in train_dnn, the number of hidden layers and neurons per layer are increased, allowing the model to extract features more effectively for fitting and the training curve becomes smoother as the number of batch sizes increases. However, after completing iterations of 72 epochs, the degradation of the network occurs, resulting in the decreasing trend of accuracy on the training set. DNN hidden layers, 6–9, are replaced with two RESNET-blocks to form a DNN + RESNET structure. Taking the best model of DNN with the most suitable hyperparameters as a reference, the DNN with RESNET architecture is trained. As a result, it is shown in Fig. 8.

From the training results in Fig. 8, the training set accuracy increases gradually with the number of iterations and tends to be stable when the number of epochs exceeds 80, indicating that the model converges well. The prediction rate on the validation set can be close to 83%, indicating that the DNN with RESNET performs well and that the model has a good level of generalization. As the number of layers and neurons
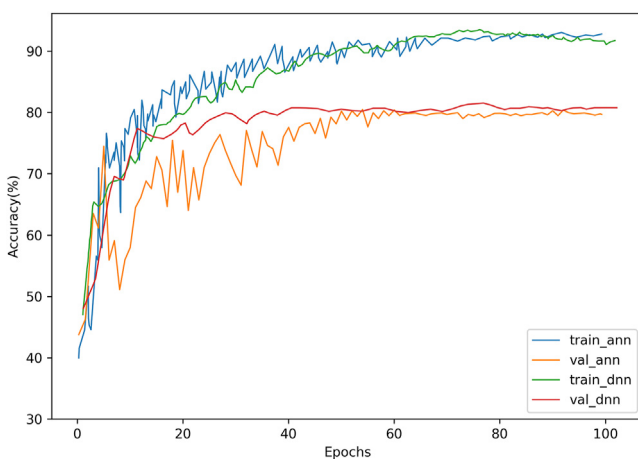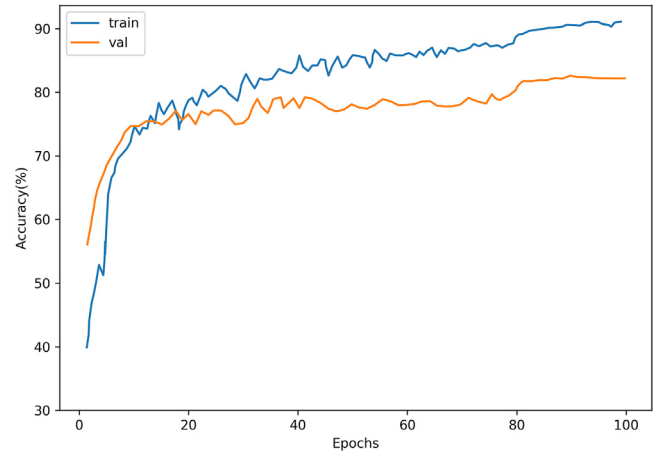
Fig. 8 – Comparison of accuracy between the training set and validation set in the DNN with RESNET.

increases, the model can extract the feature values more accurately, but the degradation of the network is still inevitable as the number of layers increases. Due to the inclusion of the residual block structure based on the original depth model, to a certain extent, the feature information can be propagated across layers and is not easily decayed, thus ultimately improving the utilization rate of feature information and the accuracy of prediction.

In addition, residual blocks are formed by adding skip connections from the first hidden layer. However, the model performed poorly. It suggests that the network design is not valid. The neural networks are integrated in an end-to-end approach in which the feature values are extracted hierarchically by the first few layers of neural networks, and the feature values are fitted for classification by the final few levels. The purpose of the residual block is to solve the gradient problem during back propagation, ensuring that what is learned in the deep network is not lost and that it continues to learn new information, improving the prediction rate. As a result, adding skip connections when the features are not fully derived is not reasonable.

With Micro-F1 to assess the prediction results, the test set is used to validate the efficacy of the three neural networks. The Micro-F1 is in the equations,

$$Recall_{micro} = \frac{\sum_{i=1}^{n} TP_i}{\sum_{i=1}^{n} TP_i + \sum_{i=1}^{n} FN_i} \tag{13}$$

$$Precision_{micro} = \frac{\sum_{i=1}^{n} TP_i}{\sum_{i=1}^{n} TP_i + \sum_{i=1}^{n} FP_i} \tag{14}$$

$$F1_{micro} = 2 \cdot \frac{Precision_{micro} \cdot Recall_{micro}}{Precision_{micro} + Recall_{micro}} \tag{15}$$

where true positive (TP_i) denotes that the positive case is correctly recognized as a positive case of the i element, false positive (FP_i) refers that the negative case is incorrectly

Fig. 7 – Comparison of accuracy between the training set and validation set with the ANN model and DNN model.

Table 3 − Micro-F1 score of ANN, DNN, and DNN with RESNET models.

Model	ANN	DNN	DNN with RESNET
TP	384	413	433
FN	145	116	96
FP	145	116	96
F1	0.726	0.781	0.819

recognized as a positive case of the i element, and false negative (FN_i) signifies that the positive case is incorrectly recognized as a negative case of the i element. $Recall_{micro}$ indicates how many of the samples that are actually positive in the sample space are correctly predicted, $Precision_{micro}$ indicates how many of the samples with positive predictions are forecasted correctly, and $F1_{micro}$ is defined as the summed average, which weighs $Precision_{micro}$ and $Recall_{micro}$. The final outcome is shown in Table 3.

As shown in Table 3, the true positive (TP_i) of DNN with RESNET is 433, and it shows that its Micro-F1 score is higher than others, reaching 0.819. This indicates that DNN with RESNET outperforms other models on the test set and enhances the learning capacity of the network at deeper levels owing to the inclusion of residual blocks, which solves network degradation to some degree and increases prediction accuracy. Fig. 9 shows that according to prior studies, DNN with RESNET outperforms the other models in terms of accuracy in predicting phase information of HEAs. Lee et al. [48] used generative adversarial networks (GAN) to augment the dataset data by creating adversarial data, achieving the average prediction rate of 93.17% based on the DNN architecture. It shows that when the sample size of the dataset is insufficient, increasing the amounts for the dataset is more effective than increasing the number of hidden layers or neurons in the neural network and optimizing the network structure.

3.3. Relative significance of input features

DNN with RESNET architecture is used to assess the relative significance of the six input features. Six experiments that
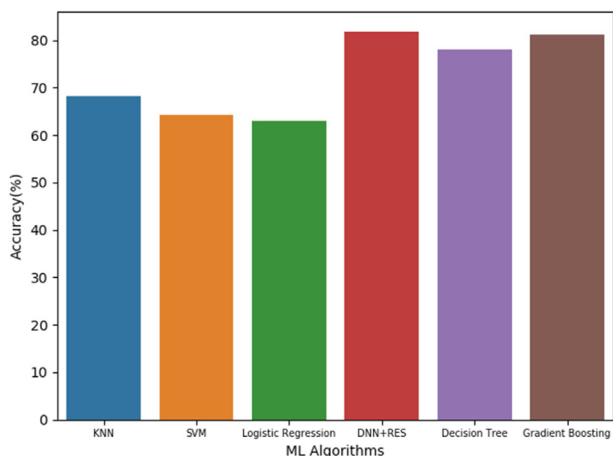
Fig. 9 − Comparison of accuracy for machine learning algorithms.
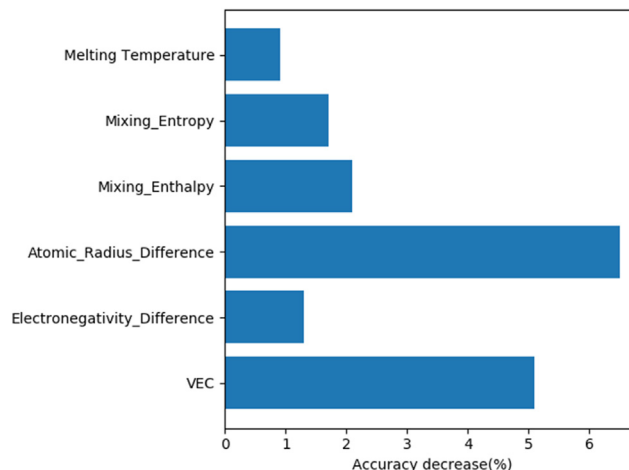
Fig. 10 − Impact of the test set accuracy when removing any feature.

delete one feature each time while keeping the other five are carried out to retrain the model and predict the outcomes to investigate the influence on the test accuracy. Fig. 10 shows the accuracy degradation with the six experiments. This means that all of the accuracy declines positively and deleting any of the six features affects test accuracy [33]. Among them, the atomic size difference and the valence electron concentration have a greater impact on the accuracy of the predicted results than the other feature values. It is found that the significant design parameters, i.e., the atomic size difference and the valence electron concentration, deduced by the current RESNET method coincide with those from the existing parametric rules for the HEA phase formation. In line with the Hume-Rothery rules, it is recognized that the atomic size difference plays a vital role in the formation of phases, especially the SS phase [26,29,34]. Furthermore, the Hume-Rothery rules suggest that the number of valence electrons per atom influences the stability of a given solid solution in metal binary systems [35,36]. Such stabilization depends on the electron density because the density of states present peaks where the Fermi sphere is in contact with the Brillouin zone limit [34]. As a result, a structure is stabilized at a certain value of the electron concentration. It means that the simple parameters related to radius and electronegativity differences, although not always decisive, are strongly indicative in HEA composition design.

4. Conclusion

In this work, a DNN structure using RESNET is proposed for the phase formation prediction of HEAs. It shows a high overall accuracy of 81.9%. The DNN with RESNET architecture is formed by connecting across layers to form a residual network block. The DNN model with RESNET supplies more prediction accuracy than the traditional DNN network on the training set, and the validation set. Compared with machine learning models, e.g., ANN and conventional DNN, its Micro-F1 score highlights the advantages of phase prediction of

HEAs. It can remarkably prevent network degradation and improve the algorithm accuracy. By removing the eigenvalues item by item, it is found that the atomic size difference and valence electron concentration are crucial for the prediction rate and should be a focus in designing HEA compositions.

Credit authorship contribution statement

Wenhan Zhu: Methodology, Investigation, Writing - original draft. Wenyi Huo: Conceptualization, Writing - review & editing, Supervision. Shiqi Wang: Methodology, Formal analysis. Xu Wang: Formal analysis. Kai Ren: Formal analysis. Shuyong Tan: Writing - review & editing. Feng Fang: Writing - review & editing. Zonghan Xie: Writing - review & editing. Jianqing Jiang: Writing - review & editing.

Declaration of Competing Interest

The authors declare that they have no known competing financial interests or personal relationships that could have appeared to influence the work reported in this paper.

Acknowledgments

REFERENCES

[1] Zhang Y, Zuo TT, Tang Z, Gao MC, Dahmen KA, Liaw PK, et al. Microstructures and properties of high-entropy alloys. Prog Mater Sci 2014;61:1–93.

[2] Gludovatz B, Hohenwarter A, Catoor D, Chang EH, George EP, Ritchie RO. A fracture-resistant high-entropy alloy for cryogenic applications. Science 2014;345:1153–8.

[3] Huo WY, Fang F, Liu XD, Tan SY, Xie ZH, Jiang JQ. Remarkable strain-rate sensitivity of nanotwinned CoCrFeNi alloys. Appl Phys Lett 2019;114:101904.

[4] Miracle DB, Senkov ON. A critical review of high entropy alloys and related concepts. Acta Mater 2017;122:448–511.

[5] Chang XJ, Zeng MQ, Liu KL, Fu L. Phase engineering of high-entropy alloys. Adv Mater 2020;32:1907226.

[6] Huo WY, Liu XD, Tan SY, Fang F, Xie ZH, Shang JK, et al. Ultrahigh hardness and high electrical resistivity in nano-twinned, nanocrystalline high-entropy alloy films. Appl Surf Sci 2018;439:222–5.

[7] Li ZM, Pradeep KG, Deng Y, Raabe D, Tasan CC. Metastable high-entropy dual-phase alloys overcome the strength-ductility trade-off. Nature 2016;534:227–30.

[8] Huo WY, Zhou H, Fang F, Hu XJ, Xie ZH, Jiang JQ. Strain-rate effect upon the tensile behavior of CoCrFeNi high-entropy alloys. Mater Sci Eng 2017;689:366–9.

[9] Huo WY, Shi HF, Ren X, Zhang JY. Microstructure and wear behavior of CoCrFeMnNbNi high-entropy alloy coating by TIG cladding. Adv Mater Sci Eng 2015:647351.

[10] Shi YZ, Collins L, Feng R, Zhang C, Balke N, Liaw PK, et al. Homogenization of AlₓCoCrFeNi high-entropy alloys with improved corrosion resistance. Corrosion Sci 2018;133:120–31.

[11] Wang SQ, Huo WY, Fang F, Xie ZH, Shang JK, Jiang JQ. High entropy alloy/C nanoparticles derived from polymetallic MOF as promising electrocatalysts for alkaline oxygen evolution reaction. Chem Eng J 2022;429:132410.

[12] Aydin F, Durgut R. Estimation of wear performance of AZ91 alloy under dry sliding conditions using machine learning methods. Trans Nonferrous Metals Soc China 2021;31:125–37.

[13] Machaka R. Machine learning-based prediction of phases in high-entropy alloys. Comput Mater Sci 2021;188:110244.

[14] Bhandari U. Yield strength prediction of high-entropy alloys using machine learning. Mater Today Commun 2021;26:101871.

[15] Huo WY, Wang SQ, Zhu WH, Zhang ZL, Fang F, Xie ZH, et al. Recent progress on high-entropy materials for electrocatalytic water splitting applications. Tungsten 2021;3:161–80.

[16] Bhandari U, Zhang CY, Zeng CY, Guo SM, Yang SZ. Deep learning-based hardness prediction of novel refractory high-entropy alloys with experimental validation. Crystals 2021;11:46.

[17] Vamsikrishna Y, Kumarjaiswal U, Rahul MR. Machine learning approach to predict new multiphase high entropy alloys[J]. Scripta Mater 2021:113804.

[18] Huang W, Martin P, Zhuang HL. Machine-learning phase prediction of high-entropy alloys. Acta Mater 2019;169:225–36.

[19] Islam N, Huang W, Zhuang HL. Machine learning for phase selection in multi-principal element alloys. Comput Mater Sci 2018;150:230–5.

[20] Borg CKH, Frey C, Moh J, Pollock TM, Saal JE. Expanded dataset of mechanical properties and observed phases of multi-principal element alloys. Sci Data 2020;7:430.

[21] Gorsse S, Nguyen MH, Senkov ON, Miracle DB. Database on the mechanical properties of high entropy alloys and complex concentrated alloys. Data Brief 2018;21:2664–78.

[22] Guo S, Liu CT. Phase stability in high entropy alloys: formation of solid-solution phase or amorphous phase. Prog Nat Sci Mater Int 2011;21:433–46.

[23] Tian F, Varga LK, Chen N, Shen J, Vitos L. Empirical design of single phase high-entropy alloys with high hardness. Intermetallics 2015;58:1–6.

[24] Tsai MH, Tsai RC, Chan T, Huang WF. Intermetallic phases in high-entropy alloys: statistical analysis of their prevalence and structural inheritance. Metals 2019;9:247.

[25] Fang SS, Xiao XS, Xia L, Li WH, Dong YD. Relationship between the widths of supercooled liquid regions and bond parameters of Mg-based bulk metallic glasses. J Non-Cryst Solids 2003;321:120–5.

[26] Zhang Y, Zhou YJ, Lin JP, Chen GL, Liaw PK. Solid-solution phase formation rules for multi-component alloys. Adv Eng Mater 2008;10:534–8.

[27] Liu CT. Physical metallurgy and mechanical properties of ductile ordered alloys (Fe, Co, Ni)₃V. Metall Rev 1984;29:168–94.

[28] Zhu JH, Liaw PK, Liu CT. Effect of electron concentration on the phase stability of NbCr₂-based Laves phase alloys. Mater Sci Eng 1997;239–240:260–4.

[29] Takeuchi A, Inoue A. Classification of bulk metallic glasses by atomic size difference, heat of mixing and period of constituent elements and its application to characterization of the main alloying element. Mater Trans 2005;46:2817–29.

[30] Byvatov E, Fechner U, Sadowski J, Schneider G. Comparison of support vector machine and artificial neural network systems for drug/nondrug classification. J Chem Inf Comput Sci 2003;43(6):1882–9.

[31] Devroye L, Gyorfi L, Lugosi G. A probabilistic theory of pattern recognition. Stoch Model Appl Probab 1996;63:194–9.

[32] Berger S. Fundamentals of machine learning for predictive data analytics: algorithms, worked examples, and case studies. Comput Rev 2016;57:282–3.

[33] Lee SY, Byeon S, Kim HS, Jin YH, Lee YS. Deep learning-based phase prediction of high-entropy alloys: optimization, generation, and explanation. Mater Des 2021:109260.

[34] Poletti MG, Battezzati L. Electronic and thermodynamic criteria for the occurrence of high entropy alloys in metallic systems. Acta Mater 2014;75:297–306.

[35] Guo S, Ng C, Lu J, Liu CT. Effect of valence electron concentration on stability of fcc or bcc phase in high entropy alloys. J Appl Phys 2011;109:103505.

[36] Mizutani U, Sato H, Massalski TB. The original concepts of the Hume-Rothery rule extended to alloys and compounds whose bonding is metallic, ionic, or covalent, or a changing mixture of these. Prog Mater Sci 2021;120:100719.